

# Methods & Extended data: Selective and Collective Actuation in Active Solids

P. Baconnier<sup>1</sup>, D. Shohat<sup>1,2</sup>, C. Hernández López<sup>3,4</sup>, C. Coulais<sup>5</sup>, V. Démery<sup>1,6</sup>, G. Düring<sup>3,4</sup>, O. Dauchot<sup>1</sup>

<sup>1</sup>*Gulliver UMR CNRS 7083, ESPCI Paris, Université PSL, 75005 Paris, France*

<sup>2</sup>*School of Physics and Astronomy, Tel-Aviv University, Tel Aviv 69978, Israel*

<sup>3</sup>*Instituto de Física, Pontificia Universidad Católica de Chile, Casilla 306, Santiago, Chile.*

<sup>4</sup>*ANID - Millenium Nucleus of Soft Smart Mechanical Metamaterials, Santiago, Chile.*

<sup>5</sup>*Van der Waals-Zeeman Institute, Institute of Physics, Universiteit van Amsterdam, Science Park 904, 1098 XH Amsterdam, the Netherlands.*

<sup>6</sup>*Univ Lyon, ENS de Lyon, Univ Claude Bernard Lyon 1, CNRS, Laboratoire de Physique, F-69342 Lyon, France.*

**Data availability.** The experimental data generated in this study have been deposited in the Zenodo database under accession code <https://doi.org/10.5281/zenodo.6653906>. The numerical data that support the findings are available from the corresponding authors upon reasonable request.

**Code availability.** All the codes supporting this study have been deposited in the Zenodo database under accession code <https://doi.org/10.5281/zenodo.6653906>.

## 1 Methods

**Experiments.** We use commercial HEXBUG nano® Nitro, highlighted in Fig. 1 of the main text. Their body length is 4 cm. The energy supply comes from a 1.5 V AG13/LR44 battery inside the robot that makes it able to vibrate and, as a consequence, to move thanks to its flexible curved legs. We embed these bugs in 3d printed cylindrical structures of 5 cm internal diameter, 3 mm thick, and 14 mm height (as the hexbugs themselves). These 3d printed annulus have 6 overhangs, that we pierced with a milling machine in order to hold the edges of the springs. Moreover, we set a thin PP plastic film on the top of the annulus to restrict the vertical motion of the hexbugs body, that we fix using commercial glue and a 3d printed 1 mm thick ring. The obtained elementary active elastic unit is shown in Fig. 1-b of the main text. These elementary components are connected by coil springs. We use two kind of springs: rigid springs RSC13 ( $k \approx 120$  N/m,  $l_0 \approx 3$  cm, external diameter 5 mm) manufactured by Ets. Jean CHAPUIS; only for the rigid body motion experiments shown in Movies 2 and 3; and soft springs ( $k \simeq 1$  N/m,  $l_0 \simeq 8$  cm, external diameter 5 mm) manufactured by Schweizer Federntechnik; for all the experiments discussed in the main text. We tune the springs stiffnesses by varying their length, the stiffness  $k$  of a coil spring being inversely proportionnal to  $l_0$ , all other parameters held constants. For the triangular lattice, kagome lattice and single particle systems, the springs lengths are respectively  $\{7.4, 6.6, 5.8, 5.0, 4.4, 3.6, 2.8\}$  cm,  $\{8.3, 7.3, 6.3, 5.5, 4.5, 3.5, 2.9, 2.2, 1.5\}$  cm and  $\{7.4, 6.7, 6.0, 5.3, 4.6, 3.9, 3.3, 2.6\}$  cm. The transitions measured in Figs. 3 and 4 of the main text were performed with constant tension of the spring's lattices. We define the tension  $\alpha$  as the ratio  $l_s/l_0$ , where  $l_0$  is the unstressed length of the springs, and  $l_s$  is the length of the springs in the stressed reference configuration. In the triangular lattice (resp. kagome lattice; resp. single particle lattice), springs are elongated by a factor  $\alpha = 1.27$  (resp.  $\alpha = 1.02$ ; resp.  $\alpha = 1.29$ ). The XY table experiments of the Supplementary Information section 2.2.2 were done with a translating stage ModuFlat P30.

**Data analysis.** The dynamics of the active elastic structures are captured with a PixeLink PL-D734MU camera, at 40 frames per second, unless otherwise stated. The obtained movies are processed with Python. The annulus barycenters defines the active units' positions  $\mathbf{r}_i(t)$ . They are detected using a Hough circle transform restricted to the annulus radius as obtained from the movies. The hexbugs body directions are obtained by computing the first moments of the image restricted to each annulus, thresholded such that only the hexbugs bodies are detected. The proper orientations are then determined by integrating  $\delta \mathbf{r}_i(t) \cdot \hat{\mathbf{n}}_i(t)$  along the dynamics, where  $\delta \mathbf{r}_i(t) = \mathbf{r}_i(t + \delta t) - \mathbf{r}_i(t)$ , and determining its sign for each hexbug. The time average oscillation frequency  $\omega_i$  of an active unit is measured by fitting the long-time behavior of  $\langle \theta_i(t + \tau) - \theta_i(t) \rangle_t(\tau)$  with linear power law, where  $\theta_i$  refers to the orientation of particle  $i$ . The collective oscillation frequency  $\Omega = \frac{1}{N} \sum_i \langle \omega_i \rangle_t$ .

**Error estimates.** Denoting the error on the detected positions  $\Delta u$ , and the annulus internal diameter  $d$ , we have  $\Delta u/d \simeq 1/20$  (because the Hough circle transform does not find perfectly the barycenters). The angles are detected modulo a typical error of  $\Delta \theta = 3^\circ$ . Using the error estimates on the detected positions and orientations, we can also have the error estimates on the displacement/polarity field projections on the normal modes. They right  $\Delta [\langle \varphi_k | \hat{\mathbf{n}} \rangle / \sqrt{N}] \simeq \Delta \theta \sqrt{Q_k}$  and  $\Delta [\langle \varphi_k | \mathbf{u} \rangle / \sqrt{N}] \simeq \Delta u \sqrt{Q_k}$  where  $Q_k = (\sum_i |\varphi_k^i|)^2 / N$  is mode  $k$ 's participation ratio, bounded between 0 and 1. As an example, for a plane-wave mode  $Q_k \simeq 0.67$ , and we find  $\Delta [\langle \varphi_k | \hat{\mathbf{n}} \rangle^2 / N] =$

$2 \frac{\langle \varphi_k | \hat{n} \rangle}{\sqrt{N}} \Delta \left[ \frac{\langle \varphi_k | \hat{n} \rangle}{\sqrt{N}} \right] \leq 2\Delta\theta\sqrt{Q_k} \simeq 0.05$ : the fraction of active force injected in a given mode is thus given modulo a typical 5% error due to tracking inaccuracies.

**Numerical simulations.** We simulate the noiseless Eqs. (1) from the main text with a Runge-Kutta method. The numerical curves shown in Figs. 2a and 4a were obtained from typically 20 random initial conditions for the polarities, and initial positions at their reference configuration, for each value of  $\pi$ . Temporal averaging takes place once a steady state is reached. The annealing simulations of Fig. 3 are initiated in the collective actuation regime. The value of  $\pi$  is varied discontinuously, by steps of 0.1, and data are time averaged once a new steady state is reached. The values of  $\pi_c^{\max}$  were found through a numerical optimization process of  $\pi_c(|\hat{n}\rangle)$  (Supplementary Information section 4).

## 2 Extended Data

**Fixed points stability analysis for the experimental structures** A given fixed point, i.e. any configuration of the polarity field, becomes unstable for  $\pi > \pi_c$ , where  $\pi_c$  is given by Eq. (S36). This stability threshold can be evaluated numerically for both experimental structures. We do so for one million configurations of the polarity field, sampled by drawing randomly and independently the orientations of each active units according to a uniform distribution in  $[0, 2\pi[$ . The results are shown in (Extended Data Figs. 1b and d), and highlight the fraction of configurations that remain stable for a given value of  $\pi$ .

As expected we find no configurations destabilizing for  $\pi < \pi_c^{\min} = \omega_{\min}^2$ , where the first configurations, locally orthogonal to the lowest energy mode, become unstable. The upper bound obtained by evaluating Eq. (S45) for all pairs of mode is not very sharp. However, we find that the pair of mode achieving the smallest bound coincides with the pair of mode on which the condensation takes place (Extended Data Figs. 1a and c).

**Large  $N$  limit** We perform numerical simulations of Eqs. (1) of the main text for triangular, respectively kagome, lattices, increasing the number of active units, up to  $N = 1141$ , respectively  $N = 930$ , while keeping  $L$  constant, with a size  $L$ , such that the lowest energy modes have unity squared eigenfrequencies. The fraction of nodes activated in the center of the system,  $f_{CA}$ , is defined as the ratio of the number of active units rotating at least 90% of the maximum rotation frequency over the total number of active units. The collective actuation oscillation frequency  $\Omega_{CA}$  is defined as the average of the individual rotation rates inside the collectively actuated region. We quantify the condensation level by computing the averaged condensation fraction in the symmetry class  $(1/2)$ ;  $\lambda_{1/2} = \frac{1}{N_{1/2}} \sum_{i \in [1/2]} \langle \langle \varphi_i | \hat{n} \rangle^2 \rangle_t$ , where  $[1/2]$  refers to the modes belonging to the  $(1/2)$  symmetry class, and  $N_{1/2}$  is the number of modes involved. This quantity, bounded between 0 and 1, is the fraction of the dynamics condensed on the selected actuated modes (Fig.3-d of the main text).

**Role of the noise** In the noiseless and overdamped framework, the collective actuation has been identified as an ordered dynamical regime, corresponding to a limit cycle. In the presence of noise, Eqs. (1) of the main text turn into coupled non-linear SDEs, that we simulate using an Euler method with fixed time step  $\delta t = 10^{-3}$ , by adding a noisy angular contribution to each polarity, drawn independently from a gaussian distribution of zero mean and variance  $2D\delta t$ . We focus on the case of the triangular lattice.

We compute the collective absolute oscillation frequency,  $|\Omega| = \frac{1}{N} \sum_i \langle |\omega_i| \rangle_t$ , where  $\langle |\omega_i| \rangle_t$  is measured by fitting the long-time behavior of  $\langle |\theta_i(t + \tau) - \theta_i(t)| \rangle_t(\tau)$  with linear power law. As seen from Extended Data Fig. 2-a there is a sharp transition at finite noise amplitude  $D_c(\pi)$ , below which collective actuation subsists. For noise level much lower than  $D_c(\pi)$ , the presence of noise only reduces the averaged angular frequency, (Extended Data Fig. 2-b). Closer to the transition, the noise also allows for stochastic inversions of the direction of rotation, restoring the chiral symmetry. (Extended Data Fig. 2-c)

**Relation to non-reciprocal matter** It was recently shown that systems composed of microscopic degrees of freedom experiencing non symmetrical interactions are prone to develop chiral phases via a specific kind of transitions, which the authors called non-reciprocal [1].

Our model system, composed of active units connected by elastic springs, is a priori a good candidate for the study of this physics. As a matter of fact its dynamics results from the coupling of  $N$  polarity vectors  $\hat{n}_i$  and  $N$  displacement vectors  $\mathbf{u}_i$ , where one can recognize two abstract species  $A$  and  $B$ . We first recall Eqs. (S49), which

govern the dynamics of a single particle in an harmonic potential:

$$\dot{R} = \pi \cos(\theta - \varphi) - \omega_0^2 R \quad (1.1)$$

$$\dot{\varphi} = \frac{\pi}{R} \sin(\theta - \varphi) \quad (1.2)$$

$$\dot{\theta} = -\omega_0^2 R \sin(\varphi - \theta) \quad (1.3)$$

where  $\varphi$  (resp.  $\theta$ ) represents the angle of the displacement (resp. polarity) vector with respect to the  $x$ -axis, and where  $R$  is the norm of the displacement vector. One sees that the phases  $\varphi$  and  $\theta$  are coupled non-symmetrically, as  $J_{\hat{n} \rightarrow \mathbf{u}} = \pi/R \neq J_{\mathbf{u} \rightarrow \hat{n}} = -\omega_0^2 R$  in such a way that for  $\pi > \pi_c$ , the phase of the displacement vector chases that of the polarity.

It is therefore likely that the macroscopic dynamics for the order parameters associated to the mean polarization and mean displacement experience the kind of transition towards a chiral phase described in [1]. More precisely the coarse grained dynamics map on the general equations describing the dynamics of two vector order parameters  $\mathbf{v}_a(t, x)$ , which serve as the starting point in [1] :

$$\partial_t \mathbf{v}_a = \mathbb{A}_{ab} \mathbf{v}_b + \mathbb{B}_{abcd} (\mathbf{v}_b \cdot \mathbf{v}_c) \mathbf{v}_d + \mathcal{O}(\nabla). \quad (2)$$

They read

$$\partial_t U = \pi \mathbf{m} + \mathcal{O}(\nabla), \quad (3.1)$$

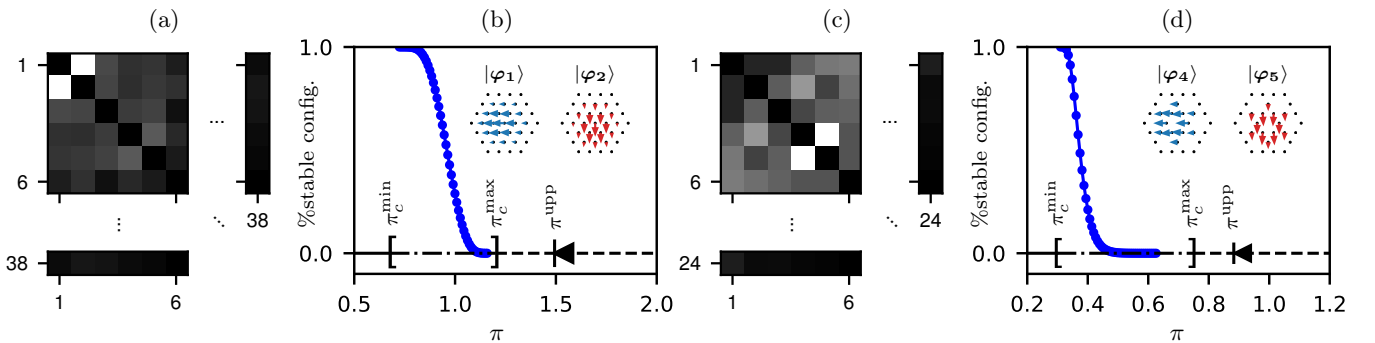
$$\partial_t \mathbf{m} = \pi \frac{1 - \mathbf{m}^2}{2} \mathbf{m} + \mathcal{O}(\nabla). \quad (3.2)$$

where the non-zero coefficients,  $\mathbb{A}_{um} = \pi$ ,  $\mathbb{A}_{mm} = \pi/2$  and  $\mathbb{B}_{mmmm} = -\pi/2$  are clearly non symmetric, opening the path to a so-called non-reciprocal phase transition.

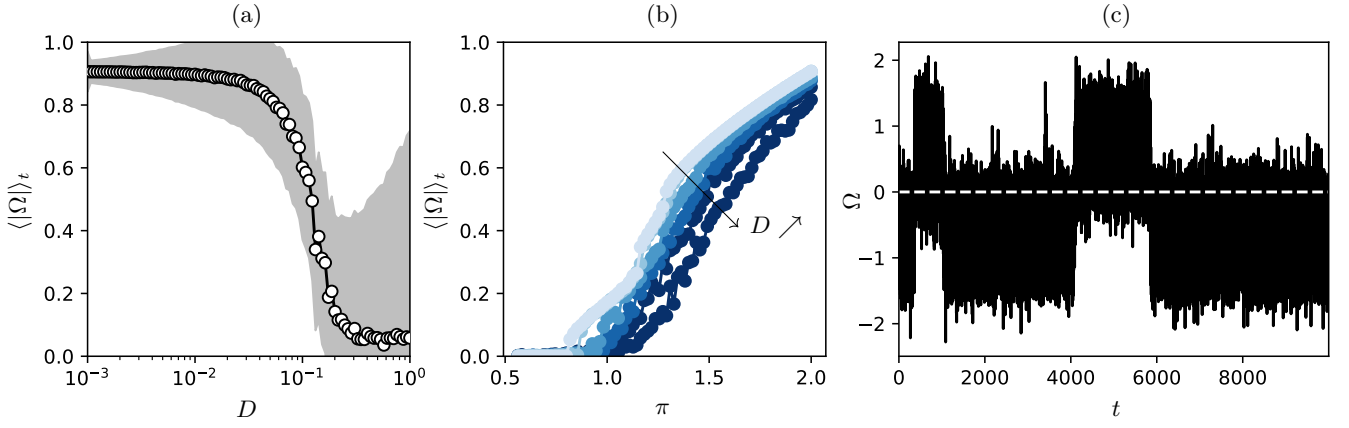
Note, however, that the transition that we observe and study is not that from an ordered (anti-)aligned phase to the chiral one. It is that from the disordered phase to the chiral one. To our knowledge this type of transition has not been, yet, investigated at the theoretical level.

## References

- [1] Fruchart, M., Hanai, R., Littlewood, P. B., Vitelli, V. Non-reciprocal phase transitions. *Nature* **592**, 363–369, (2021).



**Extended Data FIG. 1. Fixed points stability thresholds for the experimental's structures.** (a/c) Stability thresholds upper-bound  $\pi_{c,u}^{\{j,k\}}$  computed from Eq. (S45) for every pair of modes. The darker the pixel, the greater the upper-bound found. Remarkably, the best bound is always achieved for the pair of modes concerned by the condensation. (b/d) Fraction of stable fixed points as a function of  $\pi$ . The fraction of stable fixed points ( $\bullet$ ) is computed by integrating the histogram of the stability thresholds found by Eq. (S36) on one million configurations of the polarity field, drawn randomly and independently. Inset: sketch of the two most excited modes, which realized the best bound in (a/c). (a/b) For the triangular lattice pinned at the edges ( $\alpha = 1.29$ ).  $\pi_c^{\min} = 0.676$ ,  $\pi_c^{\max} = 1.20$ ,  $\pi_c^{\text{upp}} = 1.49$  (c/d) For the kagome lattice pinned at the edges ( $\alpha = 1.02$ ).  $\pi_c^{\min} = 0.375$ ,  $\pi_c^{\max} = 0.751$ ,  $\pi_c^{\text{upp}} = 0.883$ .



**Extended Data FIG. 2. Effect of the noise on the collective actuation regime.** (a) Averaged (over time) mean angular frequency (over particles) in absolute value as a function of  $D$  for  $\pi = 2.0$ . The gray area represents the  $1-\sigma$  fluctuations. (b) Averaged (over time) mean angular frequency (over particles) in absolute value as a function of  $\pi$  for increasing angular noise. From top to bottom,  $D = 0, 10^{-3}, 10^{-2}, 2 \cdot 10^{-2}, 5 \cdot 10^{-2}$ . Fluctuations are not shown for sake of clarity. (c) Mean (over particles) angular frequency as a function of time for  $\pi = 2.0$  and  $D = 10^{-1}$  in the triangular lattice pinned at the edges.